electronics

MDPI

Article

Gate-Voltage-Modulated Spin Precession in Graphene/WS_2 Field-Effect Transistors

Amir Muhammad Afzal [1,2], Muhammad Farooq Khan [3] and Jonghwa Eom [1,*]

[1] Department of Physics & Astronomy, Graphene Research Institute—Texas Photonics Center International Research Center (GRI–TPC IRC), Sejong University, Seoul 05006, Korea; Amirafzal461@gmail.com
[2] Department of Physics, Riphah International University, 13 Raiwind Road, Lahore 54000, Pakistan
[3] Department of Electrical Engineering, Sejong University, Seoul 05006, Korea; mfk.sejong@gmail.com
* Correspondence: eom@sejong.ac.kr

Abstract: Transition metal dichalcogenide materials are studied to investigate unexplored research avenues, such as spin transport behavior in 2-dimensional materials due to their strong spin-orbital interaction (SOI) and the proximity effect in van der Waals (vdW) heterostructures. Interfacial interactions between bilayer graphene (BLG) and multilayer tungsten disulfide (ML-WS_2) give rise to fascinating properties for the realization of advanced spintronic devices. In this study, a BLG/ML-WS_2 vdW heterostructure spin field-effect transistor (FET) was fabricated to demonstrate the gate modulation of Rashba-type SOI and spin precession angle. The gate modulation of Rashba-type SOI and spin precession has been confirmed using the Hanle measurement. The change in spin precession angle agrees well with the local and non-local signals of the BLG/ML-WS_2 spin FET. The operation of a spin FET in the absence of a magnetic field at room temperature is successfully demonstrated.

Keywords: spintronics; spin-orbit interaction; Hanle spin precession; graphene; spin field-effect transistor

Citation: Afzal, A.M.; Khan, M.F.; Eom, J. Gate-Voltage-Modulated Spin Precession in Graphene/WS_2 Field-Effect Transistors. *Electronics* **2021**, *10*, 2879. https://doi.org/10.3390/electronics10222879

Academic Editor: Alina Caddemi

Received: 17 October 2021
Accepted: 15 November 2021
Published: 22 November 2021

1. Introduction

An essential aim of spintronics is to exploit the spin degree of freedom of electrons to overcome challenges related to spin logic in order to develop new forms of information storage devices [1,2]. Fundamental concepts such as the creation of spin-polarized electrons and their subsequent manipulation, detection, and gate modulation have been demonstrated in spin-based devices by using electrical and optical tools. In particular, the spin field-effect transistor (FET), which plays a key role in spintronics, was proposed by Datta and Das nearly three decades ago [3–6], but spin precession of the local current controlled only by electrical methods has not yet been achieved. Elusive challenges in this field are the ability to control spin properties with back-gate voltage (V_{bg}) at ambient temperature and the development of an innovative material in which spin precession and lifetime are controlled and measured only by electrical tools [2]. However, one should note that spin-FET [7] is not an analogue of conventional semiconductor FET or MOSFET.

Graphene has a honeycomb lattice arrangement of carbon atoms, semi-metallic characteristics, and an electronic band structure featuring Dirac cones that impart unique electronic properties [8]. It is considered an excellent candidate for spin transport and spin logic devices due to its high charge carrier density, small hyperfine interactions, and long spin diffusion length [9–12]. Very small spin-orbit interaction (SOI) is an advantage of graphene for a long spin lifetime, but this makes it difficult to use as a spin channel material for spin FETs. In previous studies, various methods such as decoration of heavy metals, [13] chemical doping [14], and employment of the proximity effect [15] have been explored to enhance the SOI in graphene. Enhancement of the SOI in graphene by the proximity effect of 2-dimensional (2D) transition metal dichalcogenides (TMDs) in particular has drawn considerable research attention. TMDs have a semiconductor nature with direct or indirect

bandgaps owing to the distinct electronic structure and strong SOI, which is a few orders of magnitude larger than that of graphene [16–18]. Moreover, 2D systems with strong SOI experience Rashba-type zero-field spin splitting. Therefore, the electron spin can precess by the effective magnetic field, which is controlled by the Rashba-type SOI parameter [19]. As newly developed materials, TMDs can be used for atomically flat substrates to provide a strong SOI of ~10^2 meV, whereas the SOI of graphene is only ~10 μeV [16].

In addition, the vertically assembled heterostructure of graphene with TMDs has a proclivity to modify the interfacial interaction such that the SOI in graphene is enhanced [20,21]. Taking advantage of the proximity effect in stacked 2D materials, one can impart desirable properties on graphene without disturbing the genuine characteristics [22–27]. Recently, in our previous study [28], the WS_2/bilayer graphene (BLG)/WS_2 heterostructure exhibited a noticeable phenomenon of weak anti-localization (WAL) and zero-field spin splitting due to a strong SOI. The Rashba-type SOI strength dramatically increased from ~10 μeV to meV due to the proximity effect modulated by V_{bg} [28].

In this study, an innovative ML heterostructure of BLG/ML-WS_2 was successfully developed as a spin FET to address the challenges of injection, detection, and gate modulation of spin precession angle. Our BLG spin FET has the following distinctive features. The ferromagnetic (FM) electrodes (NiFe/AlO_x) used as source and drain contacts are patterned at 45° with respect to the BLG channel to operate the spin FET at zero external magnetic field because spins injected from the FM should have a component that is parallel to the current direction to experience the spin precession due to the Rashba-type SOI. The spin FET signals have been observed in non-local (NL) as well as local measurement configurations. Spin precession has been confirmed by the Hanle measurement. The gate modulation of spin precession in the BLG spin FET has been successfully demonstrated at 300 K. The effective spin injection, detection, and gate modulation of the graphene-based system holds great potential for applications in the field of spintronics, enabling us to discover new areas of field-effect spin transport phenomena.

2. Experimental Section

ML-WS_2 nanoflakes were mechanically exfoliated on p-type Si/SiO_2 (300 nm) substrates acting as a back-gate with the help of standard mechanical exfoliation using Scotch tape. First, we placed the BLG on top of polydimethylsiloxane (PDMS) by mechanical exfoliation from commercial graphite and transferred it onto the WS_2 flake. The thickness of BLG can be identified on the substrate because of the interference effect. Further, Raman spectroscopy and AFM were utilized to confirm the thickness. By using a micro-aligner stage, the flake of BLG was transferred onto the ML-WS_2 flake. The device was placed in a furnace for annealing at 200 °C under gas flow at a rate of 97.5% Ar/2.5% H_2 for 6 h.

To prevent direct contact of the FM electrode with WS_2, the naked areas of WS_2 were covered with 10 nm thick Al_2O_3 by atomic layer deposition (ALD). The FM electrodes were patterned by electron-beam lithography (E-beam lithography), and then aluminum (0.8 nm thick) was deposited by thermal evaporation and left to oxidize in an O_2 atmosphere for 30 m before depositing 50 nm thick $Ni_{81}Fe_{19}$ by electron-beam evaporation. A thin layer of Al_2O_3 (t = 0.8 nm) was used as a tunnel barrier between the FM electrode and the BLG to resolve conductance mismatch problems in the spin injection [29–31]. After FM deposition, the samples were placed into acetone for lift-off.

3. Results and Discussion

Figure 1a shows a schematic of the BLG/ML-WS_2 van der Waals (vdW) heterostructure spin FET; the bottom view illustrates the complete process of spin precession, and the top view represents the local measurement configuration. The widths of FM1 and FM2 were 0.3 μm and 1 μm, respectively. The width of the graphene channel was 2.3 μm. The 1 μm long BLG channel resistance was ~1.178 KΩ. A constant spin current was injected from FM1 electrode (source), and the spin signal was detected at FM2 electrode (drain). Basically,

an in-plane magnetic field ($B_{\|}$) was applied along the easy axes to align the magnetization in the same direction. The back gate voltage was applied to control the spin of electrons during the transport through the BLG channel. Figure 1b displays a scanning electron microscope image of the final device in which the FM electrode is patterned at 45° with respect to the BLG channel (the white dotted line) on WS_2. The complete optical image of the spin FET in which the WS_2 nanoflake is placed on SiO_2 (300 nm thick) serves as the dielectric gate with a highly p-doped Si wafer prepared using the mechanical exfoliation method. Subsequently, BLG was transferred to WS_2 by the dry transfer method illustrated in Figure S2a.

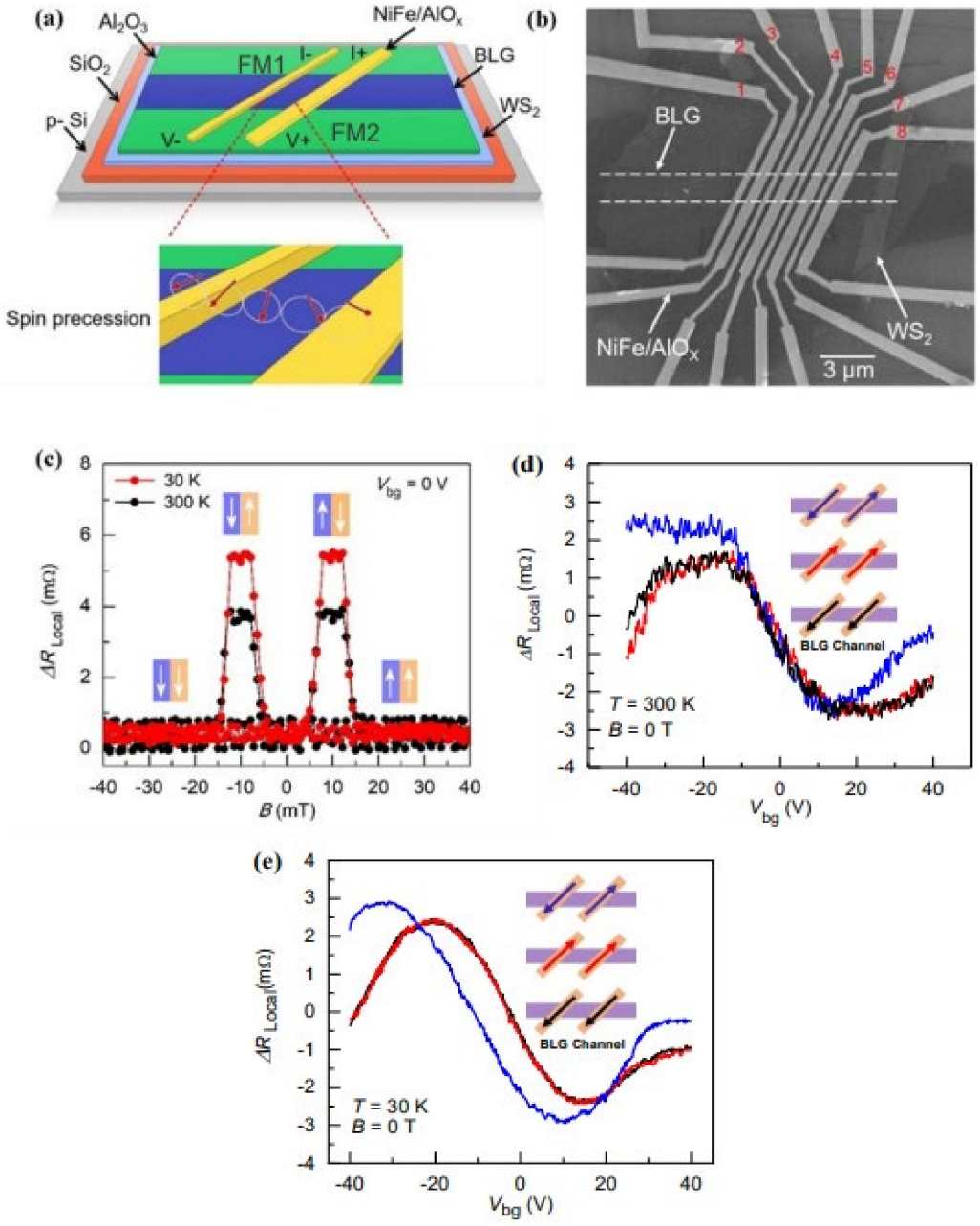

Figure 1. (**a**) Schematic representation of the BLG/ML-WS_2 spin FET. (**b**) Scanning electron microscope image of a complete BLG spin FET. (**c**) LSV signal as a function of parallel magnetic field at 300 K and 30 K at V_{bg} = 0 V, where $\Delta R_{Local} = R - R_p$ and $R_p = 1178.3\ \Omega$. (**d**) LSV signal as a function of V_{bg} at B = 0 T and at T = 300 K for anti-parallel (blue line), parallel (red line), and parallel (black line), respectively. (**e**) LSV signal as a function of V_{bg} at B = 0 T and at 30 K for anti-parallel (blue line), parallel (red line), and parallel (black line), respectively. The LSV signals are moving-averaged to remove noise from a data set.

Atomic force microscopy (AFM) was used to confirm the thickness of ML-WS_2 and BLG on SiO_2 (Figure S2b). The height profiles reveal the thickness of ML-WS_2 (~19 nm) and BLG (~0.8 nm) in Figure S2c,d, respectively. The Raman spectra of ML-WS_2 and BLG on SiO_2 are shown in Figure S3a,b, respectively. The Raman spectra of ML-WS_2 and BLG on SiO_2 are shown in Figure S3a,b. The $E_{2g}{}^1$ and A_1 peaks of WS_2 appear at 351 cm^{-1} and 418 cm^{-1}, respectively. In the case of BLG, the Raman G and 2D peaks appear around 1587 cm^{-1} and 2685 cm^{-1}, respectively. The ratio of intensities of the G to 2D peaks (I_{2D}/I_G) is ~1.2, which is consistent with the previously reported value for BLG [32]. Further, the 2D peak is fitted by four Lorentzian peaks, which confirms the nature of BLG (Figure S3c).

First, the basic electrical transport properties of Gr/WS_2 vdW heterostructure devices (sample # 2) were characterized to confirm the disappearance of the Dirac point in the case of the FM electrode. In this regard, we measured the BLG on SiO_2 and WS_2 with different contacts such as Cr/Au and NiFe, as shown in Figure S4a. In fact, the Dirac point is shifted at a higher V_{bg}~30 V due to p-type doping of BLG by NiFe electrodes.

When the BLG/WS_2 heterostructure device with FM electrode was measured, a very small change in resistance was found between $V_{bg} = -40$ V and +40 V because the bottom WS_2 layer started to conduct (Figure S4b) and behaved like a sink of the back gate electrical field at $V_{bg} > 10$ V, as shown in Figure S4c. To examine the spin valve behavior in the BLG/ML-WS_2 spin FET on SiO_2, local spin valve (LSV) measurements were conducted at room temperature (300 K) and 30 K. The local configuration is shown in Figure 1a. The local spin value measurements of the BLG/ML-WS_2 spin FET were performed by a standard lock-in technique using an AC excitation current of 9.88 μA. The spin signal was injected from one FM electrode (source) and detected from another FM electrode (drain) by applying the magnetic field (B) in the direction of the FM electrode. We applied a constant current between the two FM (7 and 8 in Figure 1b) electrodes and measured the voltage drop between these same two electrodes but opposite side contacts.

Initially, an in-plane magnetic field ($B_{\|}$) was applied along the easy axes to align the magnetization in the same direction. The FM contacts have different coercivities because they are designed with different widths (0.3 and 1 μm). The magnetization configuration of FM contacts (injector and detector) can be aligned parallel or anti-parallel by sweeping an in-plane magnetic field, which results in magnetoresistance $\left(\Delta R_{Local} = \frac{\Delta V_{Local}}{I}\right)$. A clear and noticeable local spin signal was detected at different temperatures, indicating spin transport in the BLG/ML-WS_2 spin FET (Figure 1c).

We also measured the local signal as a function of V_{bg} at different temperatures and B = 0 T for each magnetization alignment of the injector (source) and detector (drain), as shown in the inset of Figure 1d,e. For all magnetization configurations, we observed clear oscillations of the local spin signal as a function of V_{bg} at room temperature (Figure 1d). This is the first demonstration of 300 K spin FET operation. Spin FET was also demonstrated at 30 K (Figure 1e). The half oscillation angle $\left(\Delta\theta \approx 180^{\circ}\right)$ was observed for the change of back-gate voltage $\left(\Delta V_{bg} \approx 40\text{ V}\right)$ in both antiparallel and parallel states [33]. We found that the spin signal is less sensitive to V_{bg} when $V_{bg} > 10$ V. This is because ML-WS_2 is an n-type TMD semiconductor material that begins to conduct and behaves like a sink at a positive V_{bg}, where electrons start to accumulate at the surface of WS_2.

Therefore, the WS_2 film screens the back-gate electric fields. However, the charge carriers in WS_2 are much smaller than in BLG and thus contribute insignificantly to transport. In heterostructures like our BLG/ML-WS_2 spin FET, a robust local electric field is engendered by the accumulation of electrons at the interface of BLG with WS_2. The direction of this local electric field (E_z) is perpendicular to the motion of electrons. It is expected that the coupling of this local field produces a Rashba-type SOI. This kind of SOI is defined by the Rashba Hamiltonian [28]

$$H_R = \alpha \left(\vec{\sigma} \times \vec{k}_F\right) \cdot \vec{z} \quad (1)$$

where $\vec{\sigma}$ is the Pauli matrix, $\vec{k}_F$ denotes the electron wave vector, and $\vec{z}$ is a unit vector perpendicular to the interface that defines the direction of spin precession and the effective magnetic field [34,35]. In this relation, the crucial parameter (α) represents the strength of the SOI, which is directly proportional to the interfacial electric field E_z $(\alpha \propto E_z)$. The E_z of the Rashba-type SOI strength (α) originates from both the microscopic Coulomb potential and macroscopic potential gradient triggered by the hetero-interface and band bending in heterostructure devices of semiconductor materials. The macroscopic electric field can therefore be controlled by an external gate voltage applied to 2D systems and enhance the Rashba SOI [28,36]. This permits us to electrically modulate the effective magnetic field [37]. Thus, in our case, the interface of BLG with WS_2 and the proximity effect of 2D materials enhances the strength of the Rashba-type SOI [15,28,38]. To probe the spin transport behavior and pure spin current in the BLG/ML-WS_2 spin FET, an *NL* spin valve (NLSV) four-probe measurement scheme was used (Figure 2a). In order to examine the spin diffusion length (λ_s) from spin valve measurements (Figure S6a), we measured the NL signal (ΔR_{NL}) at different distances between the injector and detector (L). The NL spin value measurements of the BLG/ML-WS_2 spin FET were performed by standard lock-in technique using an AC excitation current of 9.88 μA.

For the *NL* signal (R_{NL}), a constant current was applied between the FM electrodes (7 and 8 in Figure 1b) and the NL voltage was measured at both FM contacts (6 and 5 in Figure 1b). Similar to the NL measurements, to measure the NL spin signals, we first applied a constant current and swept the $B_{\parallel}$ magnetic field along the easy axes to align the relative magnetization of the FM contacts. The difference in magnetization of the FM contacts gave rise to a sharp transition in NL magnetoresistance $\left(R_{NL} = \frac{V_{NL}}{I}\right)$ at both room temperature and 30 K. The NL signal decayed exponentially when increasing L, as shown in Figure 2b. We can evaluate λ_s by using the relation [39]

$$\Delta R_{NL} = \frac{P^2 R_t \lambda_s e^{\frac{-L}{\lambda_s}}}{2w} \tag{2}$$

where L is the spacing between the injector and detector, w is the width of the BLG channel, P is the spin polarization of the FM contacts, and R_t is the sheet resistance. By fitting the NL spin valve signal to Equation (2), we obtained λ_s and contact polarization ($\lambda_s = 0.90$ μm; P = 8.4%), as shown in Figure 2b. Further, we measured the NLSV signal as a function of V_{bg} at room temperature and 30 K (Figure 2c,d). The inset shows the alignment of magnetization for antiparallel and parallel states. Similar to the local measurement, we first used the magnetization configuration and then measured the change in R_{NL} as a function of V_{bg} at B = 0 T. We observed complete oscillation of the NLSV signal as a function of V_{bg} for each magnetization configuration of the FM electrodes. The characteristics of the oscillation in the NLSV signal are almost the same as for the local spin valve signals. The Hanle NLSV signal was measured using the configuration shown in Figure 2a.

As expected, we obtained an NL Hanle spin precession signal of $\Delta R_{NL} \approx 6.9$ mΩ with a separation of $L \approx 1$ μm (center-to-center distance) between the FM electrodes, as shown in Figure 3a. In this type of geometry, the Hanle spin signal stems from the spin precession about $B_{\perp}$ with the Larmor frequency given by $\omega_L = \frac{g\mu_B}{\hbar} B_{\perp}$, where g is the Landé factor, μ_B is the Bohr magneton, and $\hbar$ is the Planck constant divided by 2π. The variation in ΔR_{NL} due to spin precession and spin diffusion relaxation from the source to drain can be defined by

$$\Delta R_{NL} \propto \int_0^{\infty} \frac{1}{\sqrt{4\pi D_s t}} e^{-\frac{L^2}{4D_s t}} \cos(\omega_L t)\, e^{-\left(\frac{t}{\tau_s}\right)} dt \tag{3}$$

By fitting the raw data of the Hanle spin signal, we extracted the spin lifetime (τ_s) in the range of $\tau_s \approx 66.05 - 2.02$ ps depending on V_{bg}. This is in the same range of previously

reported values [40–42]. We assume that the spin diffusion constant (D_s) is the same as the charge diffusion constant (D).

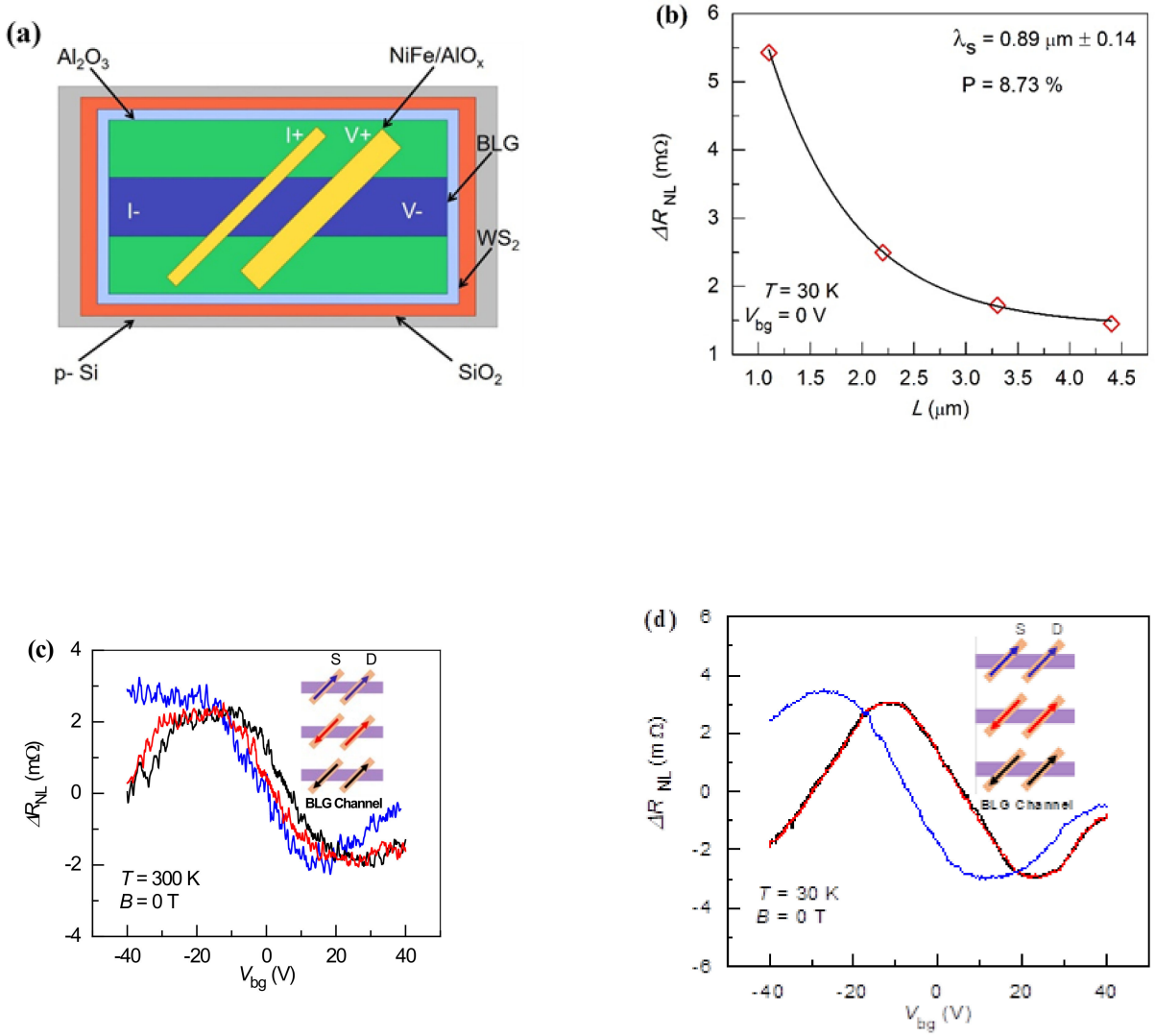

Figure 2. (**a**) *NL* measurement configuration of spin injection and detection. (**b**) Exponential decay of the NLSV signal with L of injector and detector. (**c**) NLSV spin signal as a function of V_{bg} at B = 0 T and T = 300 K for parallel (blue line), anti-parallel (red line), and anti-parallel (black line), respectively. (**d**) NLSV spin signal as a function of V_{bg} at B = 0 T and at 30 K for parallel (blue line), anti-parallel (red line), and anti-parallel (black line), respectively. The NLSV signals are moving-averaged to remove noise from a data set.

Further, we calculated the spin diffusion length ($\lambda_s = \sqrt{D_s \tau_s}$) as being in the range of $0.98 - 0.15$ μm depending on V_{bg}. The gate dependent τ_s and λ_s are shown in Figure S6a,b, respectively. Figure 3a shows the fitting of the Hanle data when V_{bg} = 0 V. The spin diffusion length estimated from the Hanle measurement (λ_s = 0.68 μm) is nearly the same as that estimated by the *NL* spin valve signal fitting (λ_s = 0.89 μm, Figure 2b). Our BLG/ML-WS_2 spin FET τ_s is very small compared to pristine graphene, which ranges from 168 to 447 ps, [43] which is indicative of the existence of a proximity-induced SOI in BLG through the WS_2 film. Such a small τ_s has also been predicted by using the spin-orbit relaxation time (τ_{so}) calculated from the spin Hall effect (SHE), WAL, and from theoretical predictions [20].

Next, we appraised the prevailing spin scattering mechanisms in our BLG/ML-WS_2 spin FET by estimating spin relaxation time (τ_s) and momentum scattering time (τ_P). First, we calculated τ_P from $D = v_F^2 \tau_P$, where v_F is the Fermi velocity. For the BLG on WS_2, we obtained D by using the Einstein relation $\sigma = e^2 D\, N_{2D}(E_F)$, where $N_{2D}(E_F)$ is the

density of states of graphene at the Fermi level [44]. In BLG, the D'yakonov-Perel' (DP) mechanism is dominant because τ_s is inversely proportional to τ_P [10,43]. Therefore, we further investigated the Rashba-type SOI using $\frac{1}{\tau_s} = \frac{4\Delta_R^2}{\hbar^2}\tau_P$. The calculated value of Δ_R (~17.15 meV) in our BLG/ML-WS_2 spin FET was much larger than the theoretically and experimentally predicted value of graphene on a conventional 2D substrates [21,42,45], which is analogous to our previous work [28].

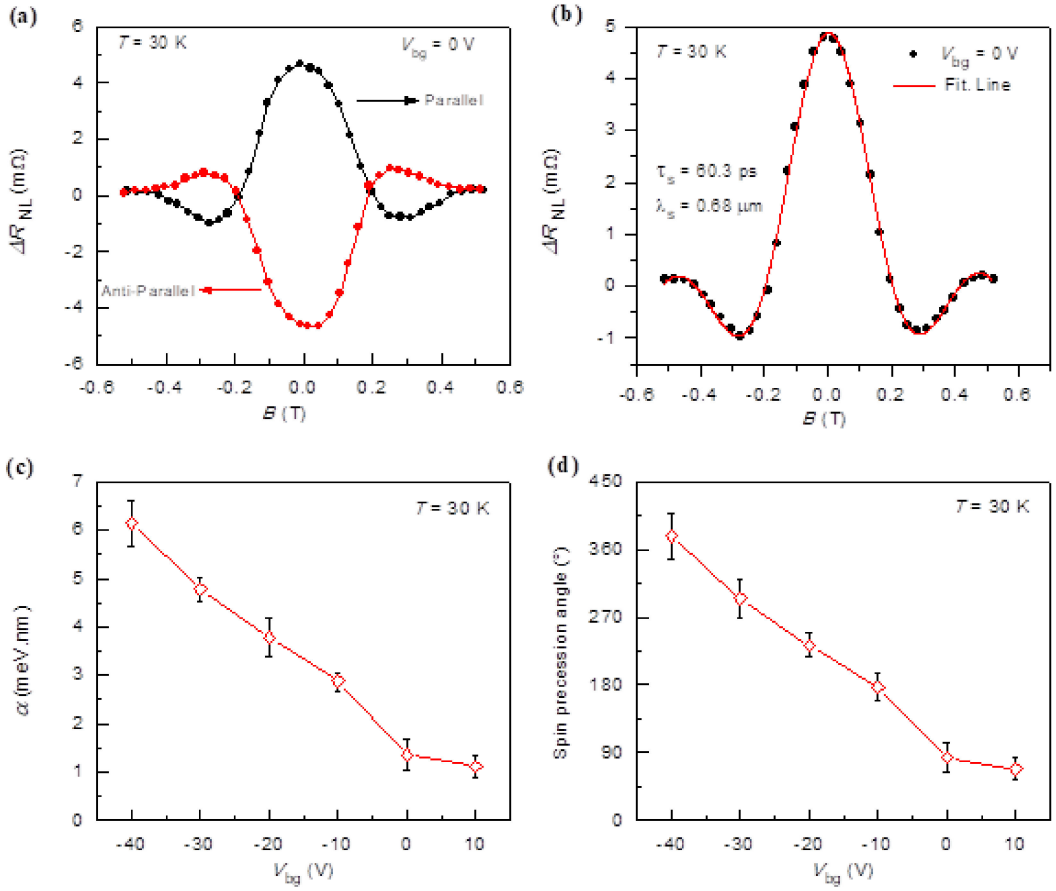

Figure 3. (**a**) Modulation of Hanle spin precession with V_{bg}. Hanle spin signal measured at different V_{bg} at 30 K. (**b**) The *NL* Hanle spin signal ($\Delta R_{NL} = R_{NL}^{Parallel} - R_{NL}^{Anti-parallel}/2$) at V_{bg} = 0 V is fitted to Equation (3) for τ_s and λ_s. (**c**) Gate voltage dependence of the SOI parameter (α). (**d**) Estimated spin precession angle as a function of V_{bg} at 30 K.

It is worthwhile noting that Δ_R can be modified by V_{bg} more effectively in BLG than in SLG; when $V_{bg} < 0$, Δ_R is more sensitive to V_{bg}, but when $V_{bg} > 0$, we found that the change in Δ_R is small due to the screening effect of gate electric fields by the n-type WS_2 film (Figure S6c). Furthermore, we calculated the Rashba-type SOI strength (α) by using the following relation [28]:

$$\tau_s = \frac{\hbar^4}{4\alpha^2 D\, m^{*\,2}} \tag{4}$$

where m^* is the effective mass of electrons and holes in BLG [46]. The estimated value of α is 6.14 meVnm, which is much higher compared to that of pristine graphene. Figure 3c shows α of the BLG/ML-WS_2 device as a function of V_{bg}. For $V_{bg} < 0$, V_{bg} efficiently changes α, whereas α does not change much when $V_{bg} > 0$ due to the screening effect of the n-type WS_2 film. Finally, from the Rashba parameter, we obtained the spin precession angle with respect to V_{bg} (Figure 3d) by the following relation [5]:

$$\Delta\theta = \frac{2m^*\alpha L}{\hbar^2} \tag{5}$$

where m^* is the effective mass of electrons and holes in BLG, $L \approx 1$ μm is separation (center-to-center distance) between the FM electrodes, and $\hbar$ is the Planck constant divided by 2π. The amount of spin precession is determined by α, which depends on V_{bg}. We have described the schematic spin precession in Figure 1a. In the BLG/ML-WS_2 spin FET, the injected spins are initially aligned in the direction of magnetization of the FM source.

In the channel, a moving electron (k_x) under an electric field (E_z) experiences an effective magnetic field (B_{Ry}) called the Rashba field. The precessional rate changes with V_{bg} because the Rashba field is proportional to E_z. When V_{bg} changes from −40 to +10 V in our BLG/ML-WS_2 spin FET, the total change of precession angle is $\Delta\theta \approx 309^\circ$ (Figure 3d). The change in precession angle is $\Delta\theta = 180^\circ$ when V_{bg} changes from −30 to 0 V, which explains the observed gate dependent local and *NL* spin signals at B = 0 T. These findings provide the first step for successfully realizing a graphene-based spin FET.

4. Conclusions

In summary, we successfully fabricated a novel BLG/ML-WS_2 spin FET to realize gate controlled spin precession. One promising outcome was the enhanced Rashba SOI in the BLG/ML-WS_2 heterostructure, as this offers the creation of a pure spin current by the SHE or the manipulation of spin through an electric field. The key parameters of spin transport (e.g., τ_s, λ_s, and α) have been derived as a function of V_{bg}. Moreover, we showed that the change of α as a function of V_{bg} explains gate controlled spin precession in the BLG/ML-WS_2 spin FET. The gate control of spin precession at room temperature is an interesting step in the field of spintronics. These outcomes may open a new platform for the manipulation of spin current, precession, and spin degree of freedom of electrons.

Supplementary Materials: The following are available online at https://www.mdpi.com/article/10.3390/electronics10222879/s1, Figure S1: Schematic diagram showing fabrication process flow of graphene/WS_2 field-effect transistors heterostructure device. (a)–(e) Schematic procedures of the device fabrication. Figure S2: Structure of the BLG/ML-WS_2 spin FET. (a) An optical microscope image of the BLG/ML-WS_2 heterostructure device with FM source and drain contact with local measurement geometry. The FM electrodes are patterned at 45° with respect to the BLG channel. The length and width of the graphene channel were 1 μm and 2.3 μm, respectively. (b) AFM image of the device showing WS_2 and BLG on SiO_2. (c) The height profile of WS_2. The thickness of the WS_2 is ~19 nm. (d) The height profile of BLG. The thickness of the BLG flake is ~0.8 nm. Figure S3: Raman spectra of the BLG/ML-WS_2 spin FET. (a) Raman spectrum of multilayers of WS_2. The peaks $E^1{}_{2g}$ and A_1 appear at 351 cm^{-1} and 418 cm^{-1}, respectively. (b) Raman spectrum of BLG. (c) Raman spectrum of BLG 2D peak. The peak is fitted by four Lorentzian peaks, which confirms the nature of BLG. Figure S4: Doping effect by NiFe electrodes and screening effect by WS_2 layer. (a) An optical image of the final device in which graphene is marked with the white dashed line on SiO_2 and WS_2 (sample #2). The different pairs of NiFe and Cr/Au electrodes were patterned by electron-beam lithography on WS_2, BLG, and BLG/WS_2 heterostructure devices, which is illustrated by purple, red, green, orange, and blue circles for WS_2 (Cr/Au), BLG (Cr/Au), BLG/WS_2 (Cr/Au), BLG/WS_2 (NiFe), and BLG (NiFe), respectively. (b) The transfer characteristics as a function of V_{bg} of WS_2 with Cr/Au (purple circle); the threshold voltage (V_{th}) was found around 10 V. (c) The resistance of BLG on SiO_2 and WS_2 as a function of back gate voltage (V_{bg}) with different electrodes. Figure S5: Gate modulation of spin precession angle in the BLG/ML-WS_2 spin FET. (a) Modulation of Hanle spin precession with back-gate voltage. Hanle spin signal measured at different back gates at 30 K. (b) Gate voltage dependence of the spin-orbit interaction parameter α. (c) Estimated spin precession angle as a function of V_{bg} at 30 K. Figure S6: Spin transport parameters. (a) Gate dependence of τ_s, which is derived from the fitting of the Hanle spin precession in Equation (3). (b) Gate dependence of λ_s. (c) Rashba spin-splitting (Δ_R) as a function of V_{bg} at 30 K. Table S1: Comparison of key parameters of bilayer graphene/multilayer WS_2 field-effect transistor with previously reported parameters in pristine graphene.

Author Contributions: A.M.A. and J.E. conceived the work, designed the research strategy, analyzed data, and wrote the paper. A.M.A. and M.F.K. performed the experiments. J.E. directed the project. All authors have read and agreed to the published version of the manuscript.

Funding: This work was supported by the grant No. 2021R1A4A1031900, the Basic Science Research Program (2019R1F1A1057697), and the Global Research and Development Center Program (2018K1A4A3A01064272) through the National Research Foundation of Korea (NRF) grant funded by the Korea government (Ministry of Education and the Ministry of Science and ICT).

Conflicts of Interest: The authors declare no conflict of interest.

References

1. Fert, A. Nobel Lecture: Origin, development, and future of spintronics. *Rev. Mod. Phys.* **2008**, *80*, 1517–1530. [CrossRef]
2. Awschalom, D.D.; Flatté, M.E. Challenges for semiconductor spintronics. *Nat. Phys.* **2007**, *3*, 153. [CrossRef]
3. Datta, S.; Das, B. Electronic analog of the electro-optic modulator. *Appl. Phys. Lett.* **1990**, *56*, 665–667. [CrossRef]
4. Chuang, P.; Ho, S.-C.; Smith, L.W.; Sfigakis, F.; Pepper, M.; Chen, C.-H.; Fan, J.-C.; Griffiths, J.P.; Farrer, I.; Beere, H.E.; et al. All-electric all-semiconductor spin field-effect transistors. *Nat. Nanotechnol.* **2014**, *10*, 35. Available online: https://www.nature.com/articles/nnano.2014.296#supplementary-information (accessed on 22 December 2014). [CrossRef] [PubMed]
5. Koo, H.C.; Kwon, J.H.; Eom, J.; Chang, J.; Han, S.H.; Johnson, M. Control of Spin Precession in a Spin-Injected Field Effect Transistor. *Science* **2009**, *325*, 1515–1518. [CrossRef] [PubMed]
6. Wunderlich, J.; Park, B.-G.; Irvine, A.C.; Zârbo, L.P.; Rozkotová, E.; Nemec, P.; Novák, V.; Sinova, J.; Jungwirth, T. Spin Hall Effect Transistor. *Science* **2010**, *330*, 1801–1804. [CrossRef] [PubMed]
7. Semenov, Y.G.; Kim, K.W.; Zavada, J.M. Spin field effect transistor with a graphene channel. *Appl. Phys. Lett.* **2007**, *91*, 153105. [CrossRef]
8. Novoselov, K.S.; Geim, A.K.; Morozov, S.V.; Jiang, D.; Zhang, Y.; Dubonos, S.V.; Grigorieva, I.V.; Firsov, A.A. Electric Field Effect in Atomically Thin Carbon Films. *Science* **2004**, *306*, 666–669. [CrossRef]
9. Wen, H.; Dery, H.; Amamou, W.; Zhu, T.; Lin, Z.; Shi, J.; Žutić, I.; Krivorotov, I.; Sham, L.J.; Kawakami, R.K. Experimental Demonstration of xor Operation in Graphene Magnetologic Gates at Room Temperature. *Phys. Rev. Appl.* **2016**, *5*, 044003. [CrossRef]
10. Han, W.; Kawakami, R.K.; Gmitra, M.; Fabian, J. Graphene spintronics. *Nat. Nanotechnol.* **2014**, *9*, 794. [CrossRef]
11. Geim, A.K.; Novoselov, K.S. The rise of graphene. *Nat. Mater.* **2007**, *6*, 183. [CrossRef]
12. Panda, J.; Ramu, M.; Karis, O.; Sarkar, T.; Kamalakar, M.V. Ultimate Spin Currents in Commercial Chemical Vapor Deposited Graphene. *ACS Nano* **2020**, *14*, 12771–12780. [CrossRef]
13. Calleja, F.; Ochoa, H.; Garnica, M.; Barja, S.; Navarro, J.J.; Black, A.; Otrokov, M.M.; Chulkov, E.V.; Arnau, A.; Vázquez de Parga, A.L.; et al. Spatial variation of a giant spin–orbit effect induces electron confinement in graphene on Pb islands. *Nat. Phys.* **2014**, *11*, 43. Available online: https://www.nature.com/articles/nphys3173#supplementary-information (accessed on 15 December 2014). [CrossRef]
14. Balakrishnan, J.; Kok Wai Koon, G.; Jaiswal, M.; Castro Neto, A.H.; Özyilmaz, B. Colossal enhancement of spin–orbit coupling in weakly hydrogenated graphene. *Nat. Phys.* **2013**, *9*, 284. Available online: https://www.nature.com/articles/nphys2576#supplementary-information (accessed on 17 March 2013). [CrossRef]
15. Avsar, A.; Tan, J.Y.; Taychatanapat, T.; Balakrishnan, J.; Koon, G.K.W.; Yeo, Y.; Lahiri, J.; Carvalho, A.; Rodin, A.S.; O'Farrell, E.C.T.; et al. Spin–orbit proximity effect in graphene. *Nat. Commun.* **2014**, *5*, 4875. Available online: https://www.nature.com/articles/ncomms5875#supplementary-information (accessed on 31 July 2014). [CrossRef]
16. Wang, Q.H.; Kalantar-Zadeh, K.; Kis, A.; Coleman, J.N.; Strano, M.S. Electronics and optoelectronics of two-dimensional transition metal dichalcogenides. *Nat. Nanotechnol.* **2012**, *7*, 699. [CrossRef]
17. Zhu, Z.Y.; Cheng, Y.C.; Schwingenschlögl, U. Giant spin-orbit-induced spin splitting in two-dimensional transition-metal dichalcogenide semiconductors. *Phys. Rev. B* **2011**, *84*, 153402. [CrossRef]
18. Xiao, D.; Liu, G.-B.; Feng, W.; Xu, X.; Yao, W. Coupled spin and valley physics in monolayers of MoS_2 and other group-VI dichalcogenides. *Phys. Rev. Lett.* **2012**, *108*, 196802. [CrossRef]
19. Nitta, J.; Akazaki, T.; Takayanagi, H.; Enoki, T. Gate Control of Spin-Orbit Interaction in an Inverted $I_{n0.53}G_{a0.47}$ $As/I_{n0.52}A_{l0.48}As$ Heterostructure. *Phys. Rev. Lett.* **1997**, *78*, 1335. [CrossRef]
20. Wang, Z.; Ki, D.K.; Chen, H.; Berger, H.; MacDonald, A.H.; Morpurgo, A.F. Strong interface-induced spin–orbit interaction in graphene on WS2. *Nat. Commun.* **2015**, *6*, 8339. Available online: https://www.nature.com/articles/ncomms9339#supplementary-information (accessed on 21 August 2015). [CrossRef]
21. Wang, Z.; Ki, D.-K.; Khoo, J.Y.; Mauro, D.; Berger, H.; Levitov, L.S.; Morpurgo, A.F. Origin and Magnitude of 'Designer' Spin-Orbit Interaction in Graphene on Semiconducting Transition Metal Dichalcogenides. *Phys. Rev. X* **2016**, *6*, 041020. [CrossRef]
22. Island, J.O.; Cui, X.; Lewandowski, C.; Khoo, J.Y.; Spanton, E.M.; Zhou, H.; Rhodes, D.; Hone, J.C.; Taniguchi, T.; Watanabe, K.; et al. Spin–orbit-driven band inversion in bilayer graphene by the van der Waals proximity effect. *Nature* **2019**, *571*, 85–89. [CrossRef] [PubMed]
23. Safeer, C.K.; Ingla-Aynés, J.; Herling, F.; Garcia, J.H.; Vila, M.; Ontoso, N.; Calvo, M.R.; Roche, S.; Hueso, L.E.; Casanova, F. Room-Temperature Spin Hall Effect in Graphene/MoS_2 van der Waals Heterostructures. *Nano Lett.* **2019**, *19*, 1074–1082. [CrossRef] [PubMed]

24. Wakamura, T.; Wu, N.J.; Chepelianskii, A.D.; Guéron, S.; Och, M.; Ferrier, M.; Taniguchi, T.; Watanabe, K.; Mattevi, C.; Bouchiat, H. Spin-Orbit-Enhanced Robustness of Supercurrent in Graphene/WS_2 Josephson Junctions. *Phys. Rev. Lett.* **2020**, *125*, 266801. [CrossRef]
25. Ingla-Aynés, J.; Herling, F.; Fabian, J.; Hueso, L.E.; Casanova, F. Electrical Control of Valley-Zeeman Spin-Orbit-Coupling–Induced Spin Precession at Room Temperature. *Phys. Rev. Lett.* **2021**, *127*, 047202. [CrossRef]
26. Omar, S.; Madhushankar, B.N.; van Wees, B.J. Large spin-relaxation anisotropy in bilayer-graphene/WS_2 heterostructures. *Phys. Rev. B* **2019**, *100*, 155415. [CrossRef]
27. Tiwari, P.; Srivastav, S.K.; Bid, A. Electric-Field-Tunable Valley Zeeman Effect in Bilayer Graphene Heterostructures: Realization of the Spin-Orbit Valve Effect. *Phys. Rev. Lett.* **2021**, *126*, 096801. [CrossRef]
28. Afzal, A.M.; Khan, M.F.; Nazir, G.; Dastgeer, G.; Aftab, S.; Akhtar, I.; Seo, Y.; Eom, J. Gate Modulation of the Spin-orbit Interaction in Bilayer Graphene Encapsulated by WS_2 films. *Sci. Rep.* **2018**, *8*, 3412. [CrossRef]
29. Rashba, E.I. Theory of electrical spin injection: Tunnel contacts as a solution of the conductivity mismatch problem. *Phys. Rev. B* **2000**, *62*, R16267–R16270. [CrossRef]
30. Schmidt, G.; Ferrand, D.; Molenkamp, L.W.; Filip, A.T.; van Wees, B.J. Fundamental obstacle for electrical spin injection from a ferromagnetic metal into a diffusive semiconductor. *Phys. Rev. B* **2000**, *62*, R4790–R4793. [CrossRef]
31. Tombros, N.; Jozsa, C.; Popinciuc, M.; Jonkman, H.T.; van Wees, B.J. Electronic spin transport and spin precession in single graphene layers at room temperature. *Nature* **2007**, *448*, 571–574. [CrossRef]
32. Ferrari, A.C.; Meyer, J.; Scardaci, V.; Casiraghi, C.; Lazzeri, M.; Mauri, F.; Piscanec, S.; Jiang, D.; Novoselov, K.; Roth, S. Raman spectrum of graphene and graphene layers. *Phys. Rev. Lett.* **2006**, *97*, 187401. [CrossRef]
33. Park, Y.H.; Choi, J.W.; Kim, H.-J.; Chang, J.; Han, S.H.; Choi, H.-J.; Koo, H.C. Complementary spin transistor using a quantum well channel. *Sci. Rep.* **2017**, *7*, 46671. [CrossRef]
34. Bychkov, Y.A.; Rashba, E.I. Oscillatory effects and the magnetic susceptibility of carriers in inversion layers. *J. Phys. C Solid State Phys.* **1984**, *17*, 6039. [CrossRef]
35. Hikami, S.; Larkin, A.I.; Nagaoka, Y. Spin-Orbit Interaction and Magnetoresistance in the Two Dimensional Random System. *Prog. Theor. Phys.* **1980**, *63*, 707–710. [CrossRef]
36. Yang, B.; Tu, M.-F.; Kim, J.; Wu, Y.; Wang, H.; Alicea, J.; Wu, R.; Bockrath, M.; Shi, J. Tunable spin–orbit coupling and symmetry-protected edge states in graphene/WS_2. *2D Mater.* **2016**, *3*, 031012. [CrossRef]
37. Roland, W. Spin-orbit coupling effects in two-dimensional electron and hole systems. In *Springer Tracts in Modern Physiscs*; Springer: Berlin/Heidelberg, Germany, 2003; p. 191.
38. Omar, S.; van Wees, B.J. Graphene-WS 2 heterostructures for tunable spin injection and spin transport. *Phys. Rev. B* **2017**, *95*, 081404. [CrossRef]
39. Matsuki, K.; Ohshima, R.; Leiva, L.; Ando, Y.; Shinjo, T.; Tsuchiya, T.; Shiraishi, M. Spin transport in a lateral spin valve with a suspended Cu channel. *Sci. Rep.* **2020**, *10*, 10699. [CrossRef]
40. Dankert, A.; Dash, S.P. Electrical gate control of spin current in van der Waals heterostructures at room temperature. *Nat. Commun.* **2017**, *8*, 16093. Available online: https://www.nature.com/articles/ncomms16093#supplementary-information (accessed on 25 May 2017). [CrossRef]
41. Omar, S.; van Wees, B.J. Spin transport in high-mobility graphene on WS_2 substrate with electric-field tunable proximity spin-orbit interaction. *Phys. Rev. B* **2018**, *97*, 045414. [CrossRef]
42. Cummings, A.W.; Garcia, J.H.; Fabian, J.; Roche, S. Giant Spin Lifetime Anisotropy in Graphene Induced by Proximity Effects. *Phys. Rev. Lett.* **2017**, *119*, 206601. [CrossRef]
43. Han, W.; Kawakami, R.K. Spin Relaxation in Single-Layer and Bilayer Graphene. *Phys. Rev. Lett.* **2011**, *107*, 047207. [CrossRef]
44. Guimarães, M.H.D.; Zomer, P.J.; Ingla-Aynés, J.; Brant, J.C.; Tombros, N.; van Wees, B.J. Controlling Spin Relaxation in Hexagonal BN-Encapsulated Graphene with a Transverse Electric Field. *Phys. Rev. Lett.* **2014**, *113*, 086602. [CrossRef]
45. Min, H.; Hill, J.E.; Sinitsyn, N.A.; Sahu, B.R.; Kleinman, L.; MacDonald, A.H. Intrinsic and Rashba spin-orbit interactions in graphene sheets. *Phys. Rev. B* **2006**, *74*, 165310. [CrossRef]
46. Zou, K.; Hong, X.; Zhu, J. Effective mass of electrons and holes in bilayer graphene: Electron-hole asymmetry and electron-electron interaction. *Phys. Rev. B* **2011**, *84*, 085408. [CrossRef]